Nano Research Energy

ISSN 2791-0091 (print); 2790-8119 (online)
https://doi.org/10.26599/NRE.2025.9120209

Research Article

Surface anchored Al-doped $Li_7La_3Zr_2O_{12}$ induced order-disorder arrangement for high-performance Li-rich layered cathodes

Jiming Peng[1], Yu Li[2], Xiaoqiong Li[3], Juncheng Huang[3], Biqun Zou[1] (✉), Fenghua Zheng[3], Qichang Pan[3], Hongqiang Wang[3], Qingyu Li[3], and Sijiang Hu[3] (✉)

[1] *Department of Chemistry and Pharmaceutical Sciences, Guilin Normal University, Guilin 541199, China*
[2] *Department of Food and Chemical Engineering, Liuzhou Institute of Technology, Liuzhou 545616, China*
[3] *Guangxi Key Laboratory of Low Carbon Energy Materials, School of Chemistry and Pharmaceutical Sciences, Guangxi Normal University, Guilin 541004, China*

Received: 7 October 2025 / **Revised:** 11 November 2025 / **Accepted:** 19 November 2025 / **Published date:** 4 January 2026

ABSTRACT

Li-rich layered oxides can provide high capacity owing to the simultaneous transition-metal cation and oxygen anion redox. However, irreversible oxygen redox usually occurs during cycling, causing structural collapse, such as the formation of nanovoids, dislocations, and phase transitions. Here, we report the design of an intergrown layered-spinel heterostructure by surface anchoring Al-doped $Li_7La_3Zr_2O_{12}$ (LLZO) nanodomains to enhance the structural stability. The Al-doped LLZO nanodomains offer a favourable ionic diffusion at the surface and significantly reduce the charge transfer resistance. The abundant local structure suppresses the nanostrain and exhibits minimal cracks in the secondary particles compared to the pristine samples. The target material delivers a discharge capacity of 295.6 mAh·g^{-1} with a Coulombic efficiency of 93.5% at 55 °C. After 200 cycles, the structural collapse was significantly reduced. This study provides new insights into the comprehensive design of the electrode/electrolyte interface for transition-metal oxides.

KEYWORDS

lithium ion battery, Li-rich layered oxide, cathode material

1 Introduction

Electric vehicles, powered by lithium-ion batteries, have been commercially available for several years. Compared with conventional petrol vehicles, however, range anxiety remains a significant concern that hinders their widespread adoption. A lack of high-energy-density electrode materials highly bottlenecks this critical shortage. Li-rich Layered oxides (LLOs) cathode materials, $Li_{1+x}M_{1-x}O_2$ ($1 < x \leq 1/3$, TM = Ni, Co, Mn, etc.), have garnered interest as they exhibit higher energy densities (~900 Wh·kg^{-1}) than traditional cathode materials, such as $LiCoO_2$, $LiNi_{1-y-z}Mn_yCo_zO_2$ ($y + z < 0.5$), $LiFePO_4$ [1–3]. Unfortunately, it remains a significant challenge, including voltage fade, capacity degradation, and unsatisfactory rate performance during the charge/discharge process [4, 5]. Such undesirable electrochemical behaviours must be overcome in these materials before achieving commercial success. These obstacles are suggested to originate from oxygen redox and cation migration, as well as the formation of dislocations [6, 7]. Oxygen redox involves both reversible and irreversible processes, with the latter characterized by oxygen release. In particular, surface lattice oxygens become more mobile and escape from TMO_6 octahedra when charged to > 4.4 V (vs. Li^+/Li), releasing oxygen into the electrolyte and forming oxygen vacancies [8–10]. These defects produced at the surface migrate into the bulk lattice, resulting in continuous structural collapse and growth throughout the particle [11–13]. Meanwhile, these vacancies formed at adjoining cation sites further form oxidized oxygen species, driving cation migration [14].

Since these issues are triggered at the surface of LLOs, surface modifications were proposed to address the challenges mentioned above. Generally, metal oxides (e.g., Al_2O_3, SnO_2) [15, 16], phosphates (Li_3PO_4, $LiFePO_4$) [17, 18], and fluorides (AlF_3, NH_4F) [19, 20], have been developed to improve the electrochemical performance of LLOs. Other surface treatments were also performed to achieve the same goal [21, 22]. For example, surface anchoring of Al-doped [23] and surface multiple treatment modification [24, 25]. We have reported a phase-compatible $La_{0.8}Sr_{0.2}MnO_{3-y}$ coating to LLO, stabilized by a surface structure that forms a heterostructural Mn-O-TM bonding network at the interface [6]. A construct spinel-layered heterostructure can offer 3D interconnected Li^+ diffusion channels and inhibit side reactions on the surface [26, 27]. In addition, fast ion conductors (Li_2SiO_3, Li_2ZrO_3) [28, 29] are considered prospective candidates for coating. Among the numerous fast ion conductors, garnet-type $Li_7La_3Zr_2O_{12}$ (LLZO) is particularly remarkable because its fast Li-

Address correspondence to Biqun Zou, 182853735@qq.com; Sijiang Hu, sjhu@gxnu.edu.cn

ion conductivity at room temperature (1 mS·cm^{-1}) and broad electrochemical window (5–6 V vs. Li/Li$^+$) [30, 31]. Therefore, LLZO has garnered intensive attention in solid-state Li-ion batteries [32, 33]. Additionally, the fast Li-ion conductivity depends on the stabilized cubic phase (another is the tetragonal phase), which can be achieved by element doping (such as the Li site with Al^{3+}, the La site with Sr^{2+}, and the Zr site with Ta^{5+}) and solid-state synthesis [34–36].

Given this, we propose an Al-doped LLZO treatment that boosts Li$^+$ conductivity at the interface of LLZO/LLO. We select $Li_{1.2}Ni_{0.13}Co_{0.13}Mn_{0.54}O_2$ (LNCM) because it is considered a typical LLO cathode material, offering extraordinary specific capacity and high cyclability [37, 38]. Herein, we demonstrate the surface anchoring of Al-doped LLZO, a fast Li-ion conductor, while inducing a spinel phase to enhance the electrochemical performance of LNCM. By employing scanning transmission electron microscopy (STEM), we identify Al-doped LLZO nanoparticles that are both anchored and integrated into a spinel phase on the LNCM surface, elucidating their influence on electrochemical performance. Profiting from high ionic conductivity originating from Al-doped LLZO and high structural stability stemming from surface spinel phase, the modified cathode displays stable capacity retention (75.0% after 200 cycles) and minor voltage fade (0.004 V per cycle).

2 Results and discussion

Figure S1 in the Electronic Supplementary Material (ESM) shows the X-ray diffraction (XRD) patterns of pristine LNCM and Al-doped LLZO treated samples. The diffraction data confirm that all samples adopt a $LiMO_2$ trigonal structure with a $R\bar{3}m$ space group (Fig. S2 in the ESM). In addition, the weak peaks between 20° and 25° indicate the existence of monoclinic Li_2MnO_3 phase ($C2/m$ space group). As previously reported [39, 40], LLOs can be refined with a trigonal ($R\bar{3}m$) $LiTMO_2$ and monoclinic ($C2/m$) Li_2MnO_3 two-phase composite. The adjacent peaks of (006)/(102) and (108)/(110) can be identified clearly, indicating that these samples have a typical layered structure. We cannot observe additional peaks until the calcined temperature increases to 700 °C. As shown in the LLZO7 sample, two weak peaks at 43.5° and 63.7° are assigned to cubic LLZO (JCPDS entry 80-0457,4) [41]. Overall, the XRD results suggest that the surface anchoring of Al-doped LLZO does not change the bulk crystal structure of LNCM. To obtain more details of surface compositions, we performed X-ray photoelectron spectroscopy (XPS) measurements (Fig. S4 in the ESM). As shown in Fig. S4(b) in the ESM, two splitting peaks are observed, which can be ascribed to Al $2p_{3/2}$ at 74.4 and 74.7 eV [42]. The peak at low binding energy can be attributed to Al^{3+} ions placed at the tetrahedral sites. While the Al $2p$ signal at higher binding energy can be ascribed to Al^{3+} ions located at the octahedral sites [43]. For the Zr $3d$ XPS spectra (Fig. S4(c) in the ESM), the peaks detected at 182.3 and 184.6 eV can be assigned to the spin-orbit of Zr $3d_{5/2}$ and Zr $3d_{3/2}$ [44]. These findings indicate the presence of Al-doped LLZO on the surface of LNCM.

As estimated from the scanning electron microscopy (SEM) images, the primary size is 100–150 nm for LNCM and 100–200 nm for LLZO6 (Figs. 1(a) and 1(b)). It is well-known that agglomerated spherical particles have a higher tap density than other shapes, which is beneficial to suppressing voltage fade [45]. The spherical secondary particles were clearly observed with a diameter of ~12 μm for LNCM and ~14 μm for LLZO6. As shown in Fig. 1(c), a characteristic d spacing of 0.47 nm for the layered (003) faces is well oriented. Similarly, LLZO6 shows a d-spacing of 0.47 nm, corresponding to the layered structure (Fig. 1(d)). In particular, we noted that the crystalline grain is inset with several amorphous areas highlighted with orange dashed lines (also marked in Fig. S5 in the ESM). These insets suggest that the LNCM particles were anchored with Al-doped LLZO nanoparticles. Of note, these particles were also observed on the surface (indicated by the white dashed line regions). When we focus on this area (Fig. 1(e)), a crystalline lattice is found parallel to the bulk layered (003) plane. The d-spacing of 0.21 nm corresponds to (532) planes of $la\bar{3}d$ structure, in agreement with the XRD results. Furthermore, the fast Fourier transformation (FFT) of Fig. 1(f) identifies the layered phase (the $R\bar{3}m$ (003) planes and $C2/m$ (022) planes) LNCM and formation of garnet-type LLZO. To confirm the uniform distribution of Al-doped LLZO, we performed scanning transmission electron microscopy (STEM)-energy dispersive spectroscopy (EDS) (Fig. 1(g)). The EDS mapping suggests that the Al-doped LLZO nanoparticles are evenly distributed at the surface of the LNCM particle.

The atomic structural changes of the LNCM after Al-doped LLZO treatment were investigated by high-angle annular dark-field (HAADF)-STEM. The pristine LNCM shows uniform contrast throughout the whole grain, corresponding to a layered structure (Fig. 2(a)). The $R\bar{3}m$ phase pattern mixed with the $C2/m$ phase is evidenced in the FFT pattern. The STEM image of LLZO6 shows Al-doped LLZO nanoparticles (orange dashed line regions) anchored on the surface of LNCM (Fig. 2(b)), which was confirmed by EDS elemental mapping (Fig. 1(g)). Figure 2(c) shows a well-grown spinel phase at the grain edge in LLZO6. As previously reported, intergrown layered-spinel phases favour fast Li$^+$ diffusion [27]. Interestingly, clear layered-spinel hetero-structures were observed at a grain boundary (Fig. 2(d) and Fig. S6 in the ESM). This atomic arrangement offers 3D channels for Li$^+$ diffusion and mitigates the lattice strain-induced structural transformation [46].

Apart from the grain edges, the spinel phase can also be observed inside the grains. Figure 3(a) shows the heterogeneous structure including structurally coherent rhombohedral $LiTMO_2$ and monoclinic Li_2MnO_3 nanodomains, as well as the spinel phase (dashed circle in FFT). The corresponding EDS elemental mappings indicate a relatively uniform Al-doped LLZO distribution at the LNCM particle (Fig. S7 in the ESM). As mentioned in the XRD results, calcining at 600 °C may not be enough to grow well-crystallized LLZO crystalline particles. In that case, we suppose that part of the Al-doped LLZO particles is amorphous. We note a bright contrast behind the spinel phase (Fig. 3(a)). Since heavy elements, such as Zr and La, have relatively bright contrast in HAADF imaging [47], the stronger contrast indicates spinel nanodomains coupling with Al-doped LLZO nanoparticles (Fig. S8 in the ESM). When focusing on the enlarged area of dotted red and purple squares (Figs. 3(b) and 3(c)), layered $LiTMO_2$, Li_2MnO_3, and spinel phases can also be observed (Fig. S9 in the ESM). These abundant local structures can be observed elsewhere (Fig. 3(d)). The order-disorder arrangement can boost a more homogeneous structure evolution during battery operation, minimizing inter-lattice strain [11]. Beyond the amorphous, we also observed crystalline Al-doped LLZO. Particle sizes ranged between 5–7 nm for Al-doped LLZO (Fig. S10 in the ESM), which is in agreement with Fig. 2(b). These LLZO nanodomains display lattice stripes with a spacing of 0.29 and 0.17 nm, corresponding to (420) and (642) planes of $la\bar{3}d$ structure.

During the first cycle, the charge curve is characterized by a

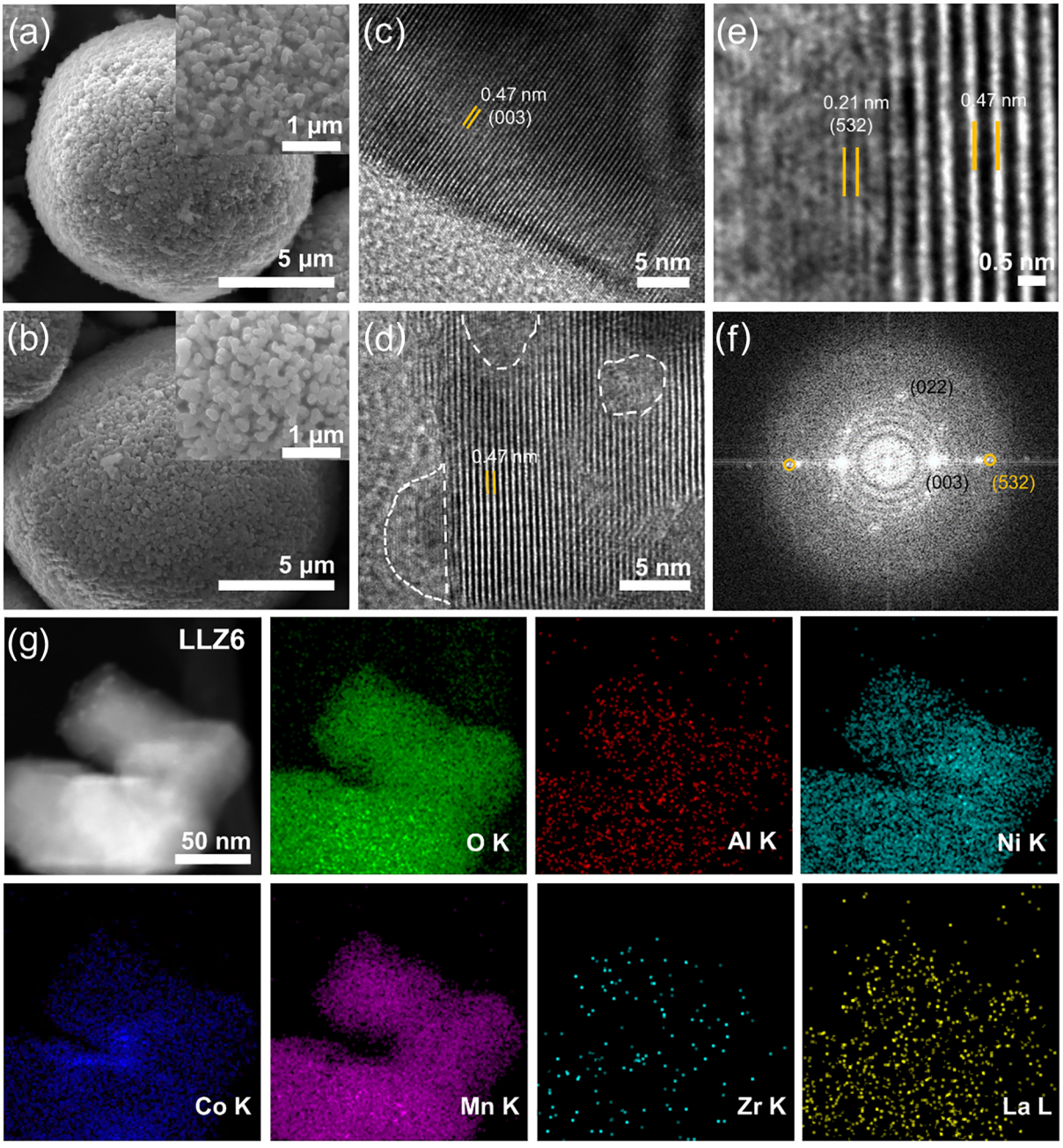

Figure 1 Morphological characterization of LNCM and LLZO6. SEM images of as-prepared LNCM (a) and LLZO6 (b). High-resolution transmission electron microscopy (HRTEM) images of LNCM (c) and LLZO6 (d). (e) The enlarged HRTEM image of the white area in (d). (f) The FFT pattern of (d). (g) STEM-EDS mapping of LLZO6.

slope below 4.4 V and a flat plateau above 4.4 V, which can be assigned to the oxidation of cations and lattice oxygen, respectively (Fig. 4(a)). This anion evolution is typically related to the activation of the Li_2MnO_3 phase and simultaneous deep delithiation in the honeycomb superstructure [48]. LNCM delivers 301.1 mAh·g^{-1} during the first discharge, whereas the modified electrodes (LLZO4, LLZO5, LLZO6, and LLZO7) exhibit 295.4, 291.9, 292.2, and 287.8 mAh·g^{-1}, respectively. The smaller discharge capacity of the modified electrodes is attributed to the inactive Al-LLZO. All samples show an initial Coulombic efficiency of around 85%. Notably, the discharge voltage decreases slightly to approximately 3.0 V. In particular, the voltage decay increases as the treatment temperature increases. As we mentioned in the XRD results, a higher calcined temperature will induce more spinel phase. Since Mn reduction mainly occurs at about this voltage, this voltage decay may originate from more Mn redox from the spinel phase and sluggish kinetics of oxygen reduction [49]. This feature can be observed in the cyclic voltammetry plot (Fig. S11 in the ESM). The LLZO6 displays evident reduction peak and oxidation peak at 2.6 and 2.8 V, corresponding to the characteristic peak of spinel. The differential capacity (dQ/dV) curves show that the two compounds display similar charge characteristics (Fig. S12 in the ESM). The charge plots were characterized by a sharp anodic peak at 4.55 V, attributed to the oxidation of lattice oxygen. The LLZ06 has a smaller peak shift during cycling, indicating a more reversible structural evolution. When cycled at 55 °C, all samples exhibit increased initial Coulombic efficiency except for LLZO4

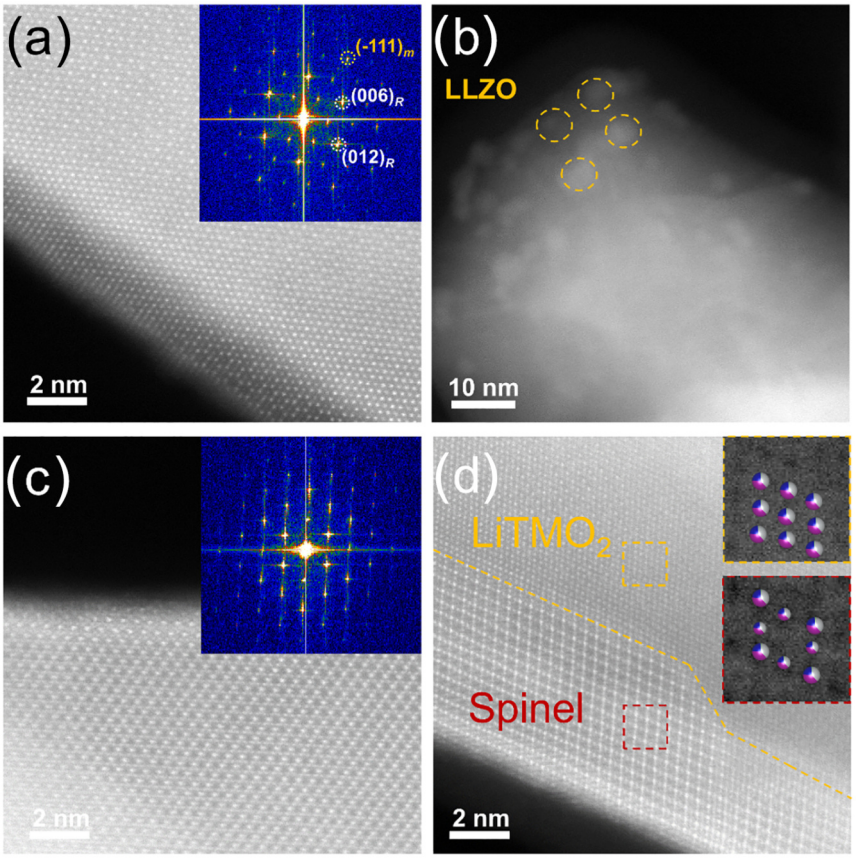

Figure 2 Local structure of LNCM and LLZO6 from STEM-HAADF. (a) STEM-HAADF image of LNCM at the surface. (b) STEM-HAADF image of LLZO6 particle. (c) STEM-HAADF image for the spinel phase of the LLZO6 particle. (d) STEM-HAADF image at the layered-spinel heterostructure for the LLZO6 particle.

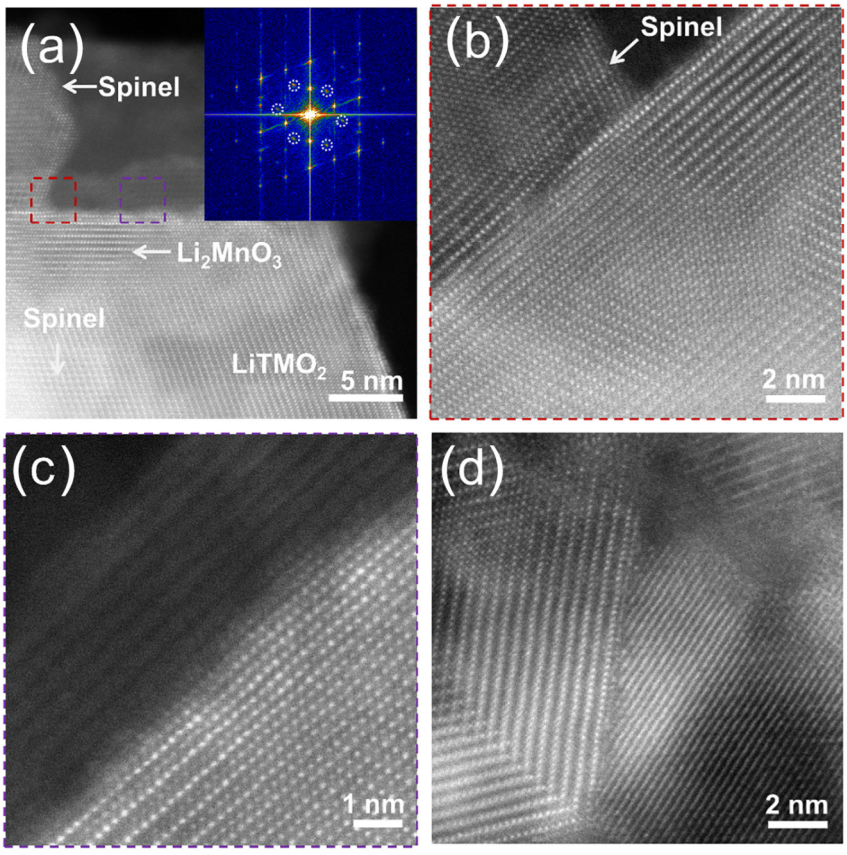

Figure 3 Local structure of LLZO6 particles. (a) STEM-HAADF image of LLZO6 grain edge. (b) The enlarged STEM-HAADF image of dotted red square in (a). (c) The enlarged STEM-HAADF image of the dotted purple square in (a). (d) STEM-HAADF image of LLZO6 grain boundaries.

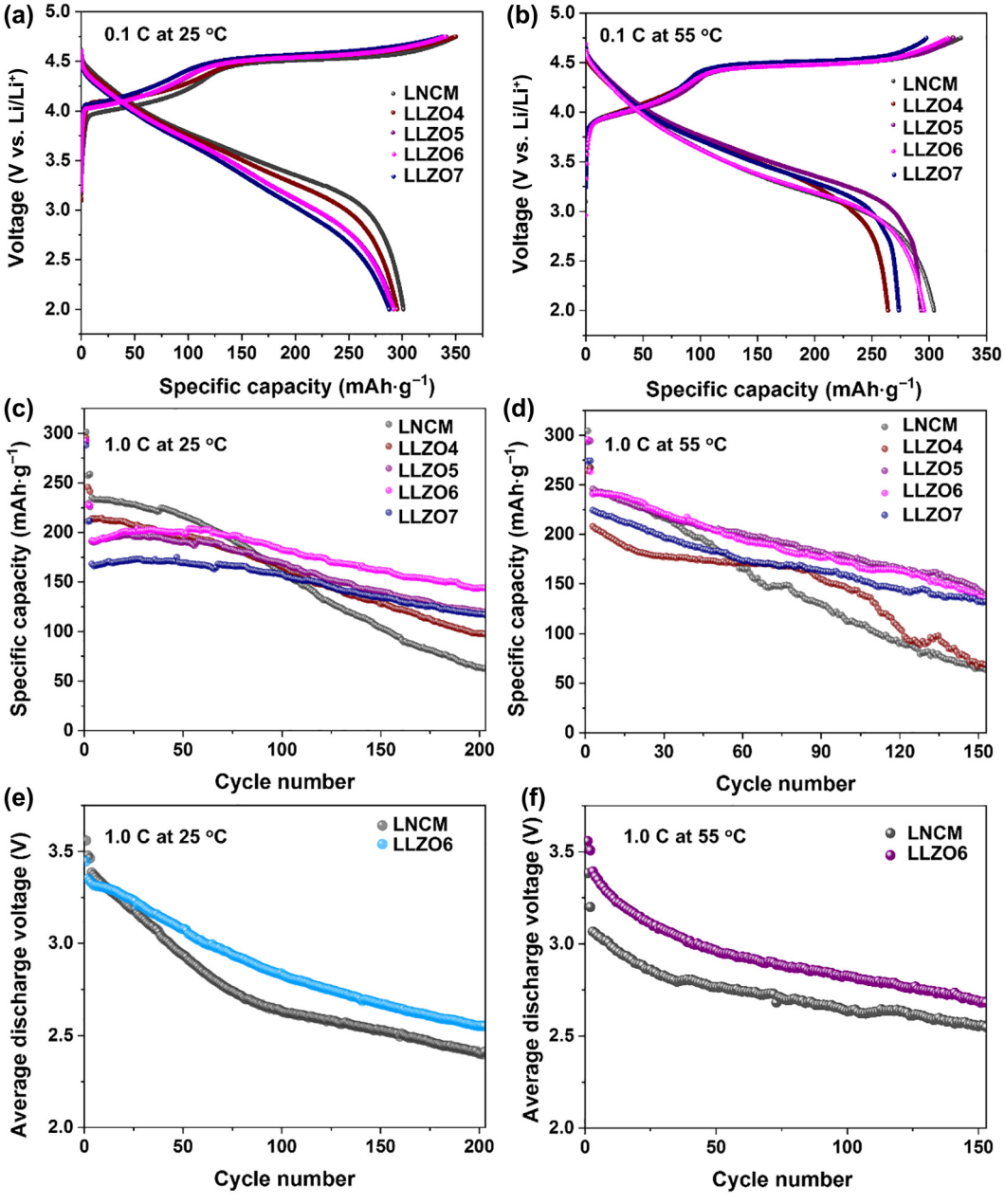

Figure 4 Electrochemical performance. (a, b) The first charge-discharge curves. (c, d) Cycle performance. (e, f) Average discharge voltage of LNCM and LLZO6 upon cycling. (a, c, e) are tested at 25 °C. (b, d, f) are tested at 55 °C.

(Fig. 4(b)). We suppose that 400 °C is not high enough to form LLZO. As a result, the low electronic and ionic conductivity of the precursor is detrimental to electrochemical performance. LNCM delivers a discharge capacity of 304.2 mAh·g^{-1} with a Coulombic efficiency of 92.9%. By contrast, LLZO6 shows a discharge capacity of 295.6 mAh·g^{-1} and a Coulombic efficiency of 93.5%. The improved Coulombic efficiency is attributed to higher reaction kinetics at elevated temperature. We note that promoting oxygen reduction mitigates the decrease in discharge voltage.

The Al-doped LLZO electrodes also exhibit enhanced cycle stability and rate performance. After activation in the first three cycles, the modified electrodes retained 45.4%, 62.8%, 75.0%, and 69.5% of their initial capacity after 200 cycles at 1.0C (Fig. 4(c)). The pristine electrode retained 26.6% of its original value under the same test conditions. More critically, all samples exhibit enhanced stability except for LLZO4 at 55 °C (Fig. 4(d)). In particular, the LLZO6 displays capacity retention of 56.0% compared with 26.0% for LNCM after 150 cycles. The modification of the Al-doped LLZO mitigates voltage fade. When measured at 25 °C, LNCM exhibits a voltage drop of 0.005 V per cycle. Whereas the LLZO6 displays suppressed voltage fade corresponding to a 0.004 V per cycle voltage drop (Fig. 4(e)). When cycled at 55 °C, the LNCM and LLZO6 show similar voltage fade (Fig. 4(f)). However, the LLZO6 exhibits a higher average discharge voltage. The higher voltage is ascribed to higher kinetics at elevated temperature [50]. After the activation in the 0.1C, the LLZO6 show improved rate capability at all C-rate compared with the pristine electrode (Fig. S13 in the ESM). The improved ionic conductivity is highlighted by electrochemical impedance spectroscopy (EIS) measurements (Figs. S14–S16, Table S1 in the ESM). The EIS spectra are characterized by a high-frequency semicircle (R_s, the resistance of the electrolyte), a mid-high frequency semicircle (R_{ct}, the charge transfer resistance), and a straight line in the low-frequency region (Z_w, the Warburg

impedance) [51]. Compared with the LNCM, the calculated Li^+ coefficient D of modified electrodes is increased. Furthermore, LLZO6 demonstrates the lowest R_{ct} among these electrodes after the first and 200th cycles. The enhanced ionic conductivity is attributed to the Al-doped fast Li^+ conductor, in which the possible routes of Li diffusion are shown in Fig. S17 in the ESM.

LLO cathodes usually undergo severe structural degradation during long-term cycling [1]. To further investigate the structural stability, *ex situ* SEM and TEM were performed on electrodes cycled for 200 cycles at 25 °C. SEM image of LNCM shows evident cracks in secondary particles (Fig. 5(a)). Dramatically, the cracks can be found elsewhere (Fig. S18(a) in the ESM). This feature suggests that LNCM experienced serious nanostrain during battery operation [4]. When evaluating the TEM images, nanovoids, dislocations, and a spinel phase are observed (Figs. 5(b) and 5(c)). By contrast, the LLZO6 displays moderate structural degradation during the 200 cycles. After cycling, the LLZO6 sample maintained a lower interface impedance and a more complete structure, indicating that the Al-doped nanodomain achieved dynamic stability by promoting ion diffusion and suppressing oxygen loss. Figure 5(d) shows more minor cracks on an LLZO6 secondary particle. When searching in a larger area, we only observed two secondary particles with cracks (Fig. S18(b) in the ESM). TEM images also show an ordered layered structure and amorphous Al-LLZO (Figs. 5(e) and 5(f)). The introduction of LLZO nanodomains reduces the surface energy, thereby promoting the densification of secondary particles. This process, in turn, mitigates stress concentration and suppresses crack propagation during cycling.

In summary, the influence of the Al-doped LLZO anchoring and layered-spinel heterostructure on the structural evolution of LNCM is illustrated in Fig. 6. It has three main advantages: 1) Boosting the ionic conductivity at the electrode/electrolyte interface. As discussed in the electrochemical performance, Al-doped LLZO possesses a fast Li^+ transport channel, thereby contributing to the interface ionic conductivity, and resulting in faster kinetics of oxygen redox. 2) Mitigating the nanostrain in the secondary particles. As illustrated in Fig. 6(a), the pristine LNCM exhibits irreversible oxygen redox, resulting in oxygen release and nanostrain. These headwinds generated structural changes, including nanovoids, dislocations, and phase transformations. Ultimately, they manifest as severe cracks among the secondary particles. 3) The surface-anchored Al-LLZO can slow down corrosion from HF, similar to commonly used surface modifications. Therefore, the structural collapse can be avoided in LLZO6 during the prolonged cycling (Fig. 6(b)).

3 Conclusions

We have constructed a robust surface structure for Li-rich layered oxides, in which an intergrown layered-spinel heterostructure was created simultaneously with anchoring Al-doped LLZO fast Li^+ conductor. The modified surface, characterized by an atomic-level abundance of local structure, enables minimal nanostrain and structural change in the surface region. Moreover, the Al-doped LLZO nanodomains offer fast Li^+ diffusion during battery operation. This study clarifies the critical influence of building diversity within local structures on improving electrochemical performance. We believe this scalable strategy provides new options for interface engineering beyond the conventional concept.

Acknowledgements

The authors acknowledge the support from the National Natural Science Foundation of China (22169004), Guangxi Natural

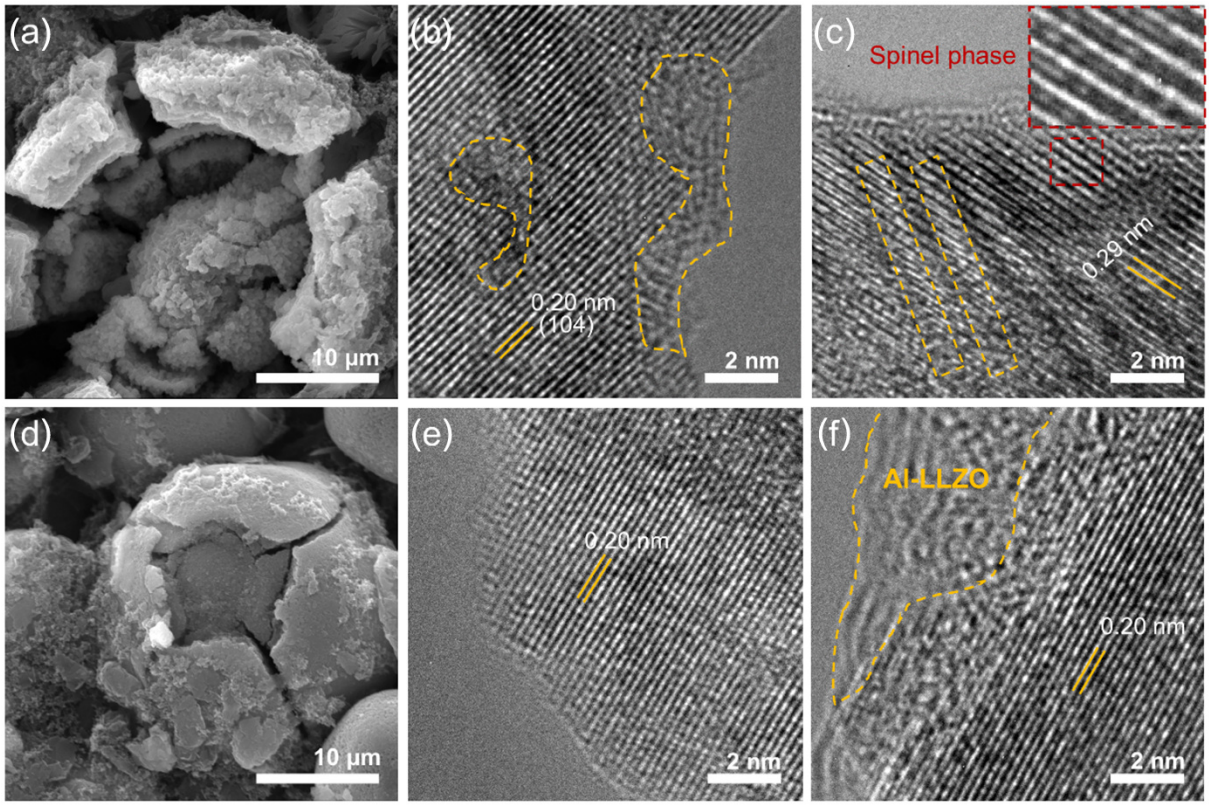

Figure 5 SEM and TEM images of the cycled electrodes. (a-c) LNCM. (d-f) LLZO.

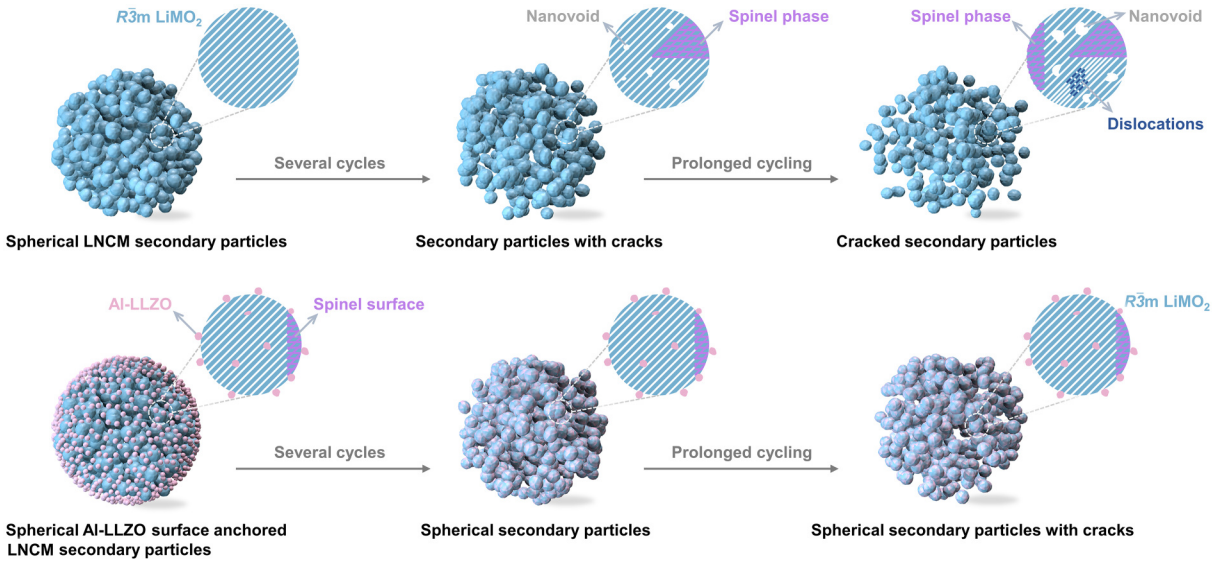

Figure 6 Schematic of structural evolution of LNCM and LLZO6 during cycling.

Science Foundation (2024GXNSFFA010003), the project of improving the basic scientific research ability of young and middle-aged teachers in Guangxi universities (2024KY0983), and Guangxi Key Laboratory of Low Carbon Energy Material (2023GXKLLCEM0102).

Electronic Supplementary Material Supplementary material (experimental procedures, XRD patterns, crystal models, TEM/STEM imaging, elemental mapping, impedance spectra, kinetic parameters, fitted resistance, lithium-ion diffusion coefficient data, SEM images of cycled electrodes) is available in the online version of this article at https://doi.org/10.26599/NRE.2025.9120209.

Declaration of conflicting interests

The authors declare no conflicting interests regarding the content of this article.

Data availability

All data needed to support the conclusions in the paper are presented in the manuscript and/or the Supplementary Materials. Additional data related to this paper may be requested from the corresponding author upon request.

References

[1] Li, X. Q.; Yu, S. L.; Peng, J. M.; Liang, L.; Pan, Q. C.; Zheng, F. H.; Wang, H. Q.; Li, Q. Y.; Hu, S. J. Fundamentals, status and promise of Li-rich layered oxides for energy-dense Li-ion batteries. *Small* **2025**, *21*, 2500940.

[2] Xu, J. H.; Wong, W. L.; Du, H.; Kang, Y. Q.; Zhao, Y.; Lan, B.; Guo, Z. Y.; Titirici, M. M.; Kang, F. Y.; Li, B. H. Upcycling the cathodes of spent lithium ion batteries into high-performance cathodes. *Nano Res. Energy* **2025**, *4*, e9120174.

[3] Payandeh, S.; Strauss, F.; Mazilkin, A.; Kondrakov, A.; Brezesinski, T. Tailoring the $LiNbO_3$ coating of Ni-rich cathode materials for stable and high-performance all-solid-state batteries. *Nano Res. Energy* **2022**, *1*, 9120016.

[4] Liu, T. C.; Liu, J. J.; Li, L. X.; Yu, L.; Diao, J. C.; Zhou, T.; Li, S. N.; Dai, A.; Zhao, W. G.; Xu, S. Y. et al. Origin of structural degradation in Li-rich layered oxide cathode. *Nature* **2022**, *606*, 305–312.

[5] Liu, H.; Hua, W. B.; Kunz, S.; Bianchini, M.; Li, H.; Peng, J. L.; Lin, J.; Dolotko, O.; Bergfeldt, T.; Wang, K. et al. Tailoring superstructure units for improved oxygen redox activity in Li-rich layered oxide battery's positive electrodes. *Nat. Commun.* **2024**, *15*, 9981.

[6] Hu, S. J.; Li, Y.; Chen, Y. H.; Peng, J. M.; Zhou, T. F.; Pang, W. K.; Didier, C.; Peterson, V. K.; Wang, H. Q.; Li, Q. Y. et al. Insight of a phase compatible surface coating for long-durable Li-rich layered oxide cathode. *Adv. Energy Mater.* **2019**, *9*, 1901795.

[7] Peng, J. M.; Li, Y.; Chen, Z. Q.; Liang, G. M.; Hu, S. J.; Zhou, T. F.; Zheng, F. H.; Pan, Q. C.; Wang, H. Q.; Li, Q. Y. et al. Phase compatible $NiFe_2O_4$ coating tunes oxygen redox in Li-rich layered oxide. *ACS Nano* **2021**, *15*, 11607–11618.

[8] Chen, Z. Q.; Kang, S. W.; Peng, J. M.; Cai, Y. J.; Huang, Y. G.; Pan, Q. C.; Zheng, F. H.; Wang, H. Q.; Li, Q. Y.; Hu, S. J. Capturing oxygen-driven electrolyte oxidation during high-voltage cycling in Li-rich layered oxide cathodes. *ACS Energy Lett.* **2023**, *8*, 417–419.

[9] Li, C.; Liu, B. W.; Jiang, N. Y.; Ding, Y. Elucidating the charge-transfer and Li-ion-migration mechanisms in commercial lithium-ion batteries with advanced electron microscopy. *Nano Res. Energy* **2022**, *1*, 9120031.

[10] Sui, C. X.; Jiang, Z. Y.; Higueros, G.; Carlson, D.; Hsu, P. C. Designing electrodes and electrolytes for batteries by leveraging deep learning. *Nano Res. Energy* **2024**, *3*, e9120102.

[11] Xu, S. Y.; Gao, Z. H.; Chen, H.; Chang, L.; Zhang, N.; Zhou, D.; Li, T. Y.; Wang, T.; Lin, C.; Xue, H. Y. et al. Minimizing inter-lattice strain to stabilize Li-rich cathode by order-disorder control. *Adv. Mater.* **2025**, *37*, 2418580.

[12] Hao, Z. K.; Gou, X. X.; Ma, H. Y.; Yang, Z.; Hao, Z. M.; Yang, G. J.; Lu, Y.; Zhao, Q.; Jin, H. F. et al. Boosting the cycle and rate performance of $Li_{1.2}Mn_{0.54}Ni_{0.13}Co_{0.13}O_2$ via single-crystal structure design. *Sci. China Mater.* **2023**, *66*, 3424–3432.

[13] Shi, C. M.; Zhu, D.; Zhang, L. W.; Song, S. Y.; Sheldon, B. W. Transfer learning prediction on lithium-ion battery heat release under thermal runaway condition. *Nano Res. Energy* **2024**, *3*, e9120147.

[14] Hong, J.; Gent, W. E.; Xiao, P. H.; Lim, K.; Seo, D. H.; Wu, J. P.; Csernica, P. M.; Takacs, C. J.; Nordlund, D.; Sun, C. J. et al. Metal-oxygen decoordination stabilizes anion redox in Li-rich oxides. *Nat. Mater.* **2019**, *18*, 256–265.

[15] Chen, W. M.; Hsieh, H. Y.; Wu, D. Z.; Tang, H. Y.; Chang-Liao, K. S.; Chi, P. W.; Wu, P. M.; Wu, M. K. Advanced TiO_2/Al_2O_3 bilayer ALD coatings for improved lithium-rich layered oxide electrodes. *ACS Appl. Mater. Interfaces* **2024**, *16*, 13029–13040.

[16] Wang, D. H.; Wang, W. L.; Li, K. H.; Song, J. Z.; Yuan, X. H.; Huang, Q. H.; Tang, Z. X.; Fu, L. J.; Wu, Y. P. Low-temperature tolerant lithium-rich manganese-based cathode enabled by facile SnO_2 decoration. *J. Mater. Chem. A* **2024**, *12*, 14467–14478.

[17] Lei, T. X.; Cao, B.; Fu, W. B.; Shi, X. L.; Ding, Z. Y.; Zhang, Q.;

Wu, J. W.; Li, K. K.; Zhang, T. Y. A Li-rich layered oxide cathode with remarkable capacity and prolonged cycle life. *Chem. Eng. J.* **2024**, *490*, 151522.
[18] Zheng, F. H.; Yang, C. H.; Xiong, X. H.; Xiong, J. W.; Hu, R. Z.; Chen, Y.; Liu, M. L. Nanoscale surface modification of lithium-rich layered-oxide composite cathodes for suppressing voltage fade. *Angew. Chem., Int. Ed.* **2015**, *54*, 13058–13062.
[19] Zhang, J. L.; Zhang, D.; Wang, Z. S.; Zheng, F.; Zhong, R.; Hong, R. Y. AlF_3 coating improves cycle and voltage decay of Li-rich manganese oxides. *J. Mater. Sci.* **2023**, *58*, 4525–4540.
[20] Hu, X.; Guo, H. J.; Wang, J. X.; Wang, Z. X.; Li, X. H.; Hu, Q. Y.; Peng, W. J. Structural and electrochemical characterization of NH_4F-pretreated lithium-rich layered $Li[Li_{0.2}Ni_{0.13}Co_{0.13}Mn_{0.54}]O_2$ cathodes for lithium-ion batteries. *Ceram. Int.* **2018**, *44*, 14370–14376.
[21] Zhao, Y. S.; Wang, F. F.; Wang, J. C.; Wang, P. F.; Yi, T. F.; Zhang, J. H. Rapid lithium-ion insertion/extraction and migration behavior of Na_2WO_4-encapsulated lithium-rich layered oxide cathode. *Rare Met.* **2024**, *43*, 3647–3660.
[22] Huang, Q. Q.; Qiu, K.; Xiao, Z. G.; Li, D. Q.; Deng, H.; Wen, L. H.; Yuan, W. J.; Peng, W.; Zhang, P.; Liu, J. Q. et al. Self-grading and surface-preservation to enhance the compaction density and structural stability of Li-rich Mn-based cathode. *Adv. Funct. Mater.* **2025**, *35*, 2422663.
[23] Su, Y. F.; Zhao, J. Y.; Dong, J. Y.; Shi, Q.; Hao, J. N.; Li, W. B.; Bao, L. Y.; Lu, Y.; Li, N.; Cao, D. Y. et al. Atomic pins bridging integrated surface to assist high-rate stability for Co-free Li-rich cathode. *Chem. Eng. J.* **2023**, *475*, 145991.
[24] Zhao, J. Y.; Su, Y. F.; Dong, J. Y.; Shi, Q.; Lu, Y.; Li, N.; Wang, H. Y.; Fang, Y. Y.; Li, W. B.; Hao, J. N. et al. Regulating anionic redox reversibility in Li-rich layered cathodes via diffusion-induced entropy-assisted surface engineering. *Energy Storage Mater.* **2024**, *70*, 103550.
[25] Zhang, H. Y.; Dong, J. Y.; Chen, G.; Che, H. Q.; Yan, K.; Wang, X.; Liu, J. Z.; Liu, D. W.; Lu, Y.; Li, N. et al. Trifunctional surface engineering of lithium-rich manganese-based oxides via Al^{3+}/PO_4^{3-} co-doping and oxygen vacancy regulation for high-performance lithium-ion batteries. *Chem. Eng. J.* **2025**, *506*, 159902.
[26] Xie, H. X.; Cui, J. X.; Yao, Z.; Ding, X. K.; Zhang, Z. H.; Luo, D.; Lin, Z. Revealing the role of spinel phase on Li-rich layered oxides: A review. *Chem. Eng. J.* **2022**, *427*, 131978.
[27] Fang, Y. Y.; Zhao, J. Y.; Su, Y. F.; Dong, J. Y.; Lu, Y.; Li, N.; Wang, H. Y.; Wu, F.; Chen, L. Understanding of spinel phases in lithium-rich cathode for high-energy-density lithium-ion batteries: A review. *Energy Mater. Adv.* **2024**, *5*, 0115.
[28] Nie, X. K.; Xu, Z.; Chen, L. N.; Li, J. W.; Cheng, J.; Sun, Q.; Qiao, Y.; Xu, X. Y.; Zhang, Y. M.; Li, D. P. et al. Enhanced electrochemical performance of $Li_{1.2}[Mn_{0.54}Co_{0.13}Ni_{0.13}]O_2$ enabled by synergistic effect of $Li_{1.5}Na_{0.5}SiO_3$ modification. *Adv. Mater. Interfaces* **2020**, *7*, 2000378.
[29] Song, B. H.; Li, W. D.; Oh, S. M.; Manthiram, A. Long-life nickel-rich layered oxide cathodes with a uniform Li_2ZrO_3 surface coating for lithium-ion batteries. *ACS Appl. Mater. Interfaces* **2017**, *9*, 9718–9725.
[30] Thompson, T.; Yu, S.; Williams, L.; Schmidt, R. D.; Garcia-Mendez, R.; Wolfenstine, J.; Allen, J. L.; Kioupakis, E.; Siegel, D. J.; Sakamoto, J. Electrochemical window of the Li-ion solid electrolyte $Li_7La_3Zr_2O_{12}$. *ACS Energy Lett.* **2017**, *2*, 462–468.
[31] Murugan, R.; Thangadurai, V.; Weppner, W. Fast lithium ion conduction in garnet-type $Li_7La_3Zr_2O_{12}$. *Angew. Chem., Int. Ed.* **2007**, *46*, 7778–7781.
[32] Ma, J.; He, R. L.; Jiang, Y. D.; Zhang, L. D.; Xu, H. L.; Zeng, H. B.; Wang, C. Y.; Xu, X. X.; Deng, Y. H.; Wang, J. et al. *In situ* coating Li_3PO_4 on $Li_{6.5}La_3Zr_{1.5}Ta_{0.5}O_{12}$ achieving lithium dendrites inhibition and high chemical stability. *Battery Energy* **2025**, *4*, e70009.
[33] Yu, W.; Deng, N. P.; Feng, Y.; Feng, X. F.; Xiang, H. Y.; Gao, L.; Cheng, B. W.; Kang, W. M.; Zhang, K. Understanding multi-scale ion-transport in solid-state lithium batteries. *eScience* **2025**, *5*, 100278.
[34] Rettenwander, D.; Redhammer, G.; Preishuber-Pflügl, F.; Cheng, L.; Miara, L.; Wagner, R.; Welzl, A.; Suard, E.; Doeff, M. M.; Wilkening, M. et al. Structural and electrochemical consequences of Al and Ga cosubstitution in $Li_7La_3Zr_2O_{12}$ solid electrolytes. *Chem. Mater.* **2016**, *28*, 2384–2392.
[35] Dumon, A.; Huang, M.; Shen, Y.; Nan, C. W. High Li ion conductivity in strontium doped $Li_7La_3Zr_2O_{12}$ garnet. *Solid State Ionics* **2013**, *243*, 36–41.
[36] Li, Y. T.; Han, J. T.; Wang, C. A.; Xie, H.; Goodenough, J. B. Optimizing Li^+ conductivity in a garnet framework. *J. Mater. Chem.* **2012**, *22*, 15357–15361.
[37] Luo, K.; Roberts, M. R.; Hao, R.; Guerrini, N.; Pickup, D. M.; Liu, Y. S.; Edström, K.; Guo, J. H.; Chadwick, A. V.; Duda, L. C. et al. Charge-compensation in 3*d*-transition-metal-oxide intercalation cathodes through the generation of localized electron holes on oxygen. *Nat. Chem.* **2016**, *8*, 684–691.
[38] Assat, G.; Iadecola, A.; Foix, D.; Dedryvère, R.; Tarascon, J. M. Direct quantification of anionic redox over long cycling of Li-rich NMC via hard X-ray photoemission spectroscopy. *ACS Energy Lett.* **2018**, *3*, 2721–2728.
[39] Mohanty, D.; Huq, A.; Payzant, E. A.; Sefat, A. S.; Li, J. L.; Abraham, D. P.; Wood, D. L.; Daniel, C. Neutron diffraction and magnetic susceptibility studies on a high-voltage $Li_{1.2}Mn_{0.55}Ni_{0.15}Co_{0.10}O_2$ lithium ion battery cathode: Insight into the crystal structure. *Chem. Mater.* **2013**, *25*, 4064–4070.
[40] Hu, S. J.; Pillai, A. S.; Liang, G. M.; Pang, W. K.; Wang, H. Q.; Li, Q. Y.; Guo, Z. P. Li-rich layered oxides and their practical challenges: Recent progress and perspectives. *Electrochem. Energy Rev.* **2019**, *2*, 277–311.
[41] Buschmann, H.; Dölle, J.; Berendts, S.; Kuhn, A.; Bottke, P.; Wilkening, M.; Heitjans, P.; Senyshyn, A.; Ehrenberg, H.; Lotnyk, A. et al. Structure and dynamics of the fast lithium ion conductor "$Li_7La_3Zr_2O_{12}$". *Phys. Chem. Chem. Phys.* **2011**, *13*, 19378–19392.
[42] Zhu, Z. R.; Zhao, Q. D.; Li, X. Y.; Li, H.; Tade, M.; Liu, S. M. Photocatalytic performances and activities in Ag-doped $ZnAl_2O_4$ nanorods studied by FTIR spectroscopy. *Catal. Sci. Technol.* **2013**, *3*, 788–796.
[43] Duan, X. L.; Yuan, D. R.; Yu, F. P. Cation distribution in Co-doped $ZnAl_2O_4$ nanoparticles studied by X-ray photoelectron spectroscopy and ^{27}Al solid-state NMR spectroscopy. *Inorg. Chem.* **2011**, *50*, 5460–5467.
[44] Li, B.; Wu, W. B.; Zhang, T. Y.; Jiang, S.; Chen, X. W.; Zhang, G. H.; Zhang, X. Ferrocene particles incorporated into Zr-based metal-organic frameworks for selective phenol hydroxylation to dihydroxybenzenes. *RSC Adv.* **2017**, *7*, 38691–38698.
[45] Li, B.; Zhang, K.; Yang, Y. L.; Zuo, Y. X.; Li, X.; Xia, D. G. Perspectives on the practicability of Li-rich NMC layered oxide cathodes. *Adv. Mater.* **2024**, *36*, 2400259.
[46] Zhang, Y.; Shi, X. Y.; Zheng, S. H.; Ouyang, Y. G.; Li, M. R.; Meng, C. X.; Yu, Y.; Wu, Z. S. Alternate heterogeneous superlattice control of lattice strain to stabilize Li-rich cathode. *Energy Environ. Sci.* **2023**, *16*, 5043–5051.
[47] Okunishi, E.; Ishikawa, I.; Sawada, H.; Hosokawa, F.; Hori, M.; Kondo, Y. Visualization of light elements at ultrahigh resolution by STEM annular bright field microscopy. *Microsc. Microanal.* **2009**, *15*, 164–165.
[48] Zheng, C. L.; Wang, Y. Q.; Mao, H. C.; Zhang, J.; Yang, X. X.; Li, J.; Zhang, D.; Wang, X. D.; Kang, F. Y.; Li, J. L. Superexchange interaction regulates Ni/Mn spin states triggering Ni-t_{2g}/O-2*p* reductive coupling enabling stable lithium-rich cathode. *Nat. Commun.* **2025**, *16*, 3900.
[49] Zhang, Z. J.; Li, Y. X.; Shen, X.; Yang, L.; Zhang, C.; Liu, Y.; Wang, B. W.; Kuo, C. Y.; Haw, S. C.; Chen, C. T. et al. Breaking the vicious spiral to suppress oxygen loss in Li-rich oxide cathode materials. *Adv. Mater.* **2025**, *37*, 2505724.
[50] Xu, J.; Sun, M. L.; Qiao, R. M.; Renfrew, S. E.; Ma, L.; Wu, T. P.; Hwang, S.; Nordlund, D.; Su, D.; Amine, K. et al. Elucidating anionic oxygen activity in lithium-rich layered oxides. *Nat. Commun.* **2018**, *9*, 947.
[51] Li, T. G.; Chen, B. T.; Wang, T. H.; Liu, C.; Yin, W.; Mao, Q. J.; Zhou, D. X.; Hao, Y. M.; Liu, X. F. Achieving stable and high-rate quasi-solid-state sodium batteries through strengthened P–O covalency and interface modification in $Na_3Zr_2Si_2PO_{12}$. *Nat. Commun.* **2025**, *16*, 5668.

Jiming Peng received her Ph.D. at Guangxi Normal University. She is now an associate research fellow at Guilin Normal University. Her research focuses on developing advanced materials and technologies for lithium-ion batteries and sodium ion batteries.

Biqun Zou received her PhD at Guangxi Normal University. Since 2019, she has been a professor at the School of Chemistry and Life Health, Guilin Normal University. Her current research focuses on inorganic chemistry. She also serves as a reviewer for the European Journal of Medicinal Chemistry.

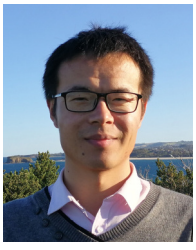

Sijiang Hu received his M.Sc. in Physical Chemistry at Guangxi Normal University and a Ph.D. from the China University of Geosciences. In 2017, he moved to the Institute for Superconducting and Electronic Materials (ISEM), University of Wollongong (UOW), as a postdoctoral research fellow with Professor Zaiping Guo. He has been a professor at the School of Chemistry and Pharmaceutical Sciences, Guangxi Normal University, since 2019. His current research interests focus on Li-ion batteries and Na-ion batteries). He is currently a young editorial board member of several major international journals, including *eScience*, *Rare Metals*, and *Nano Research Energy*.